

Geophysical Research Letters[®]



RESEARCH LETTER

10.1029/2023GL104860

Key Points:

- Substorms result in up to 21% observed ozone loss in the polar mesosphere
- This is the first observational evidence of ozone loss following substorms
- Substorm precipitation is not currently explicitly included in Energetic particle precipitation proxies for models

Supporting Information:

Supporting Information may be found in the online version of this article.

Correspondence to:

A. Seppälä,
annika.seppala@otago.ac.nz

Citation:

Chapman-Smith, K., Seppälä, A., Rodger, C. J., Hendy, A., & Forsyth, C. (2023). Observed loss of polar mesospheric ozone following substorm-driven electron precipitation. *Geophysical Research Letters*, 50, e2023GL104860. <https://doi.org/10.1029/2023GL104860>

Received 5 JUN 2023
Accepted 25 AUG 2023

Author Contributions:

Conceptualization: Keeta Chapman-Smith, Annika Seppälä
Formal analysis: Keeta Chapman-Smith
Investigation: Keeta Chapman-Smith, Annika Seppälä
Methodology: Keeta Chapman-Smith, Annika Seppälä
Supervision: Annika Seppälä
Visualization: Keeta Chapman-Smith
Writing – original draft: Keeta Chapman-Smith, Annika Seppälä
Writing – review & editing: Keeta Chapman-Smith, Annika Seppälä

© 2023 The Authors.

This is an open access article under the terms of the [Creative Commons Attribution-NonCommercial License](https://creativecommons.org/licenses/by/4.0/), which permits use, distribution and reproduction in any medium, provided the original work is properly cited and is not used for commercial purposes.

Observed Loss of Polar Mesospheric Ozone Following Substorm-Driven Electron Precipitation

Keeta Chapman-Smith¹, Annika Seppälä¹ , Craig J. Rodger¹ , Aaron Hendy¹ , and Colin Forsyth² 

¹Department of Physics, University of Otago, Dunedin, New Zealand, ²UCL Mullard Space Science Laboratory, Dorking, UK

Abstract Several drivers cause precipitation of energetic electrons into the atmosphere. While some of these drivers are accounted for in proxies of energetic electron precipitation (EEP) used in atmosphere and climate models, it is unclear to what extent the proxies capture substorm-induced EEP. The energies of these electrons allow them to reach altitudes between 55 and 95 km. EEP-driven enhanced ionization is known to result in production of HO_x and NO_x, which catalytically destroy ozone. Substorm-driven ozone loss has previously been simulated, but has not been observed before. We use mesospheric ozone observations from the Microwave Limb Sounder and Global Ozone Monitoring by Occultation of Stars instruments, to investigate the loss of ozone during substorms. Following substorm onset, we find reductions of polar mesospheric (~76 km) ozone by up to 21% on average. This is the first observational evidence demonstrating the importance of substorms on the ozone balance within the polar atmosphere.

Plain Language Summary Substorms are events in Earth's space environment that result in electrons being pushed into the Earth's atmosphere. Here, we report the first satellite observations showing that these events result in loss of polar mesospheric ozone, by up to 21%.

1. Introduction

Energetic particle precipitation (EPP) into the Earth's atmosphere can occur due to many different processes taking place in the Sun and in Earth's magnetosphere. Solar Proton Events (SPEs) are a sporadic source of high fluxes of energetic proton precipitation and are known to have a large impact on the atmosphere (Jackman et al., 2009). In addition, the Earth's magnetosphere and radiation belts are an important source of energetic electron precipitation (EEP) (Nesse Tyssøy et al., 2016; Turunen et al., 2009), contributing to the total EPP (SPE + EEP). EEP ionizes the atmosphere, resulting in increased production of HO_x and NO_x gases, both of which catalytically destroy atmospheric ozone (Turunen et al., 2009). Andersson, Verronen, Rodger, Clilverd, and Seppälä (2014) have reported up to 90% ozone depletion at mesospheric altitudes following EEP events, highlighting the importance of improved understanding of both the sources of EEP, and their atmospheric impacts.

While there has been a growing interest in EEP, some sources of electron precipitation have thus far received less focus than others. One such source of EEP are substorms. Substorms are disturbances occurring within the magnetosphere which lead to conditions for electrons to be energized, scattered and then lost into the atmosphere (Forsyth et al., 2015; Rodger et al., 2016; Rodger, Clilverd, et al., 2022; Rodger, Hendry, et al., 2022). There are three key sections to a substorm: reconnection of the magnetotail, current disruption in the near-Earth magnetic field and auroral break up (Angelopoulos, 2008). These precise mechanisms and order of events within the magnetosphere that trigger substorms remain under investigation (Angelopoulos, 2008; Cresswell-Moorcock et al., 2013).

From the EEP perspective, substorms are likely to be important due to their occurrence rate: substorm events are frequent, occurring hundreds, even thousands, of times each year (Gjerloev, 2012; Newell & Gjerloev, 2011a, 2011b; Rodger et al., 2016). The frequency of substorms does follow the solar cycle, increasing during solar maximum. The typical length of a substorm event is 1–3 hr (Akasofu, 1964; Angelopoulos et al., 2020). While the range of electron flux and peak energy of substorms have been studied, the specific fluxes of electrons entering the atmosphere and their peak energies for each individual substorm are not well known and will likely vary between substorms.

The energy of an electron that precipitates into the atmosphere determines how far down it can reach, and thus the altitude at which the peak energy is deposited. The exact energy range at which substorms trigger electrons to precipitate is still unclear due to slightly differing sources. However, it is likely that precipitating electrons' energy can range from tens of eV to as high as 1 MeV (Cresswell-Moorcock et al., 2013; Wing et al., 2013). This suggests that substorm-driven electron precipitation could impact the atmosphere as far as 65 km (Turunen et al., 2009), or even further to 50 km (Fang et al., 2008).

Simulations by Seppälä et al. (2015) found that substorms could impact the polar mesospheric ozone concentration, with simulated ozone loss at altitudes 75–85 km ranging between 5% and 50%. Observational evidence for this, however, has thus far not been presented and is the focus of the current work.

Within the mesosphere, the ozone reduction relating to particle precipitation is dominated by HO_x (see e.g., Andersson, Verronen, Rodger, Clilverd, & Wang, 2014; Seppälä et al., 2006; Sofieva et al., 2009). As HO_x has a lifetime of only a few hours, the depletion of mesospheric ozone is typically also short lived (Jackman et al., 2001). NO_x plays a smaller role in the depletion of ozone in the mesosphere, while dominating EPP driven ozone loss below 60 km (Friederich et al., 2014; Prather, 1981; Sagi et al., 2017). There is a strong seasonal dependence, since the presence of sunlight results in ample ozone production taking place, quickly replacing any loss. Hence, the maximum impact on ozone from any form of EPP is typically found during polar winter (Seppälä et al., 2015).

Ozone plays an important role in linking EPP to climate variability (Andersson, Verronen, Rodger, Clilverd, & Seppälä, 2014; Seppälä et al., 2014). Due to a lack of EEP observations, proxies using Dst and Ap indices have been developed for inclusion of EPP in atmospheric and climate modeling (i.e., Matthes et al., 2017; Nesse Tyssøy et al., 2022; van de Kamp et al., 2016). The inclusion of substorm induced precipitation into the proxies is limited to few models (Nesse Tyssøy et al., 2022). As a result, their impact on mesospheric ozone levels may be underestimated in long term simulation studies.

Following from the simulation results of Seppälä et al. (2015), in this study we use satellite observations to look for evidence of substorm precipitation impact on polar atmospheric ozone balance.

2. Data and Methods

To assess the impact of substorms on atmospheric ozone, and also provide additional confidence in the analysis, we use ozone measurements from two independent satellite instruments. The first instrument is the Microwave Limb Sounder (MLS) on-board the Aura-satellite, launched in 2004 (Schwartz et al., 2020). MLS ozone (volume mixing ratio, vmr) observations (version 5.0) cover the vertical pressure range of 261–0.001 hPa (approximately 10–94 km), with a latitudinal range of 82°N–82°S. The vertical resolution in the mesosphere is between 3.5 and 5.5 km. The years of data used from the MLS instrument is 2004–2018.

Secondly, we use mesospheric nighttime ozone observations from the Global Ozone Monitoring by Occultation of Stars (GOMOS) instrument on-board the Envisat satellite (Kyrölä et al., 2004; Tamminen et al., 2010), operational from 2002 to 2012. GOMOS ozone observations (number density, molecules cm⁻³) cover the altitude range of 15–100 km. The stellar occultation technique provides a different polar geographic coverage to that of MLS, and GOMOS has a higher mesospheric vertical resolution at ~3 km. For this analysis, we have only used stars with temperature ≥6000 K, as recommended by Tamminen et al. (2010). For nighttime conditions, the solar zenith angle at the tangent point was restricted to >107°. GOMOS observations are used for the period 2003–2011, providing some overlap with MLS. Note that the GOMOS observations cover the peak and declining phases of solar cycle 23, while MLS extends later in time to further cover the less active solar cycle 24.

We adjust both ozone data sets for seasonal trends by subtracting monthly means from the daily means following the approach used by Denton et al. (2018).

In order to identify specific substorm onset times and dates, we use the Substorm Onsets and Phases from Indices of the Electrojet (SOPHIE) substorm database, with 90% expansion percentile threshold (Forsyth et al., 2015). The SOPHIE database covers the time period from 1969 to present day. Using the information provided within the SOPHIE data set, the timing of the expansion phase (phase = 2) (Forsyth et al., 2015) is used for each substorm within the analysis as the onset timing. The SOPHIE database specifically provides the exact times and

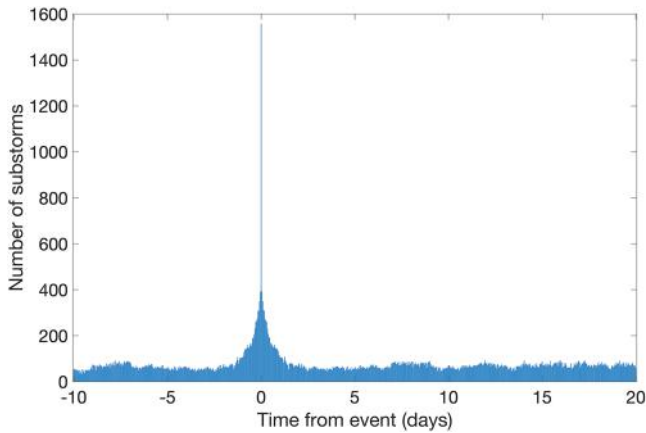


Figure 1. Number of substorm events with $AE \geq 500$ nT within the epoch period. Epoch Day 0 corresponds to the peak of 1,558 substorm events. Only substorms during the Northern Hemisphere and Southern Hemisphere polar winter seasons are considered. The histogram shows the number of substorms per hour.

dates of substorm events, rather than an activity index which would need to be interpreted for identification of substorm events.

We exclude any substorms in which the expansion phase occurs within the same day as the peak flux of an SPE, as SPE's are expected to have a large impact on the atmosphere (e.g., Funke et al., 2011).

It is reasonable to assume that only substorms or substorm clusters that will result in a significant precipitating electron flux would result in a detectable impact on the atmosphere (see e.g., Partamies et al., 2021). While there are no long term electron flux observations that could be used here, and there are no standard measures for the relative sizes of substorms that would tell us about the electron fluxes, geomagnetic activity indices have been successfully used as a proxy for EEP levels in general (see e.g., Funke et al., 2014). Thus here, we will use the hourly averaged geomagnetic Auroral Electrojet (AE) index (Davis & Sugiura, 1966; Kauristie et al., 2017) as a proxy for the potential EEP levels in combination with the SOPHIE substorm database. Newell and Gjerloev (2011a) and Lockwood et al. (2019) have shown evidence pointing to the predictive ability of the AE index when it comes to the amount of electron flux from substorms. Furthermore, Nesse Tyssøy et al. (2021) recently showed that large daily averaged AE leads to higher daily averaged EEP. The AE index has previously been used in atmospheric studies for example, by

Sinnhuber et al. (2016). The AE index is based on observations from the Northern Hemisphere (NH) at geomagnetic latitudes 60° – 70° and covers the time period from 1957 to 2018.

To identify which substorms are likely driving large electron fluxes into the atmosphere, we will apply an AE threshold of 500 nT. Similar threshold ($AE > 500$ nT) has previously been used by Zhang et al. (2018) and Aryan et al. (2016). As indicated by the statistical study of substorms of Partamies et al. (2013), the applied AE index threshold will exclude small substorms, which typically are associated with much lower AE indices.

Times when the hourly AE index reaches or passes this threshold will be cross referenced with the SOPHIE substorm database to see if a substorm has occurred within the same hour.

In order to investigate the substorm signal in the ozone observations, superposed epoch analysis (SEA, also known as compositing) has been used. Similar technique has previously been applied in EPP atmospheric impact studies for example, by Andersson, Verronen, Rodger, Clilverd, and Seppälä (2014), Friederich et al. (2014), and Denton et al. (2018). When a substorm within this time interval is identified, ozone data in the 10 days before the onset, and in the following 20 days after the onset are analyzed. This is to ensure a quiet period before onset, as well as a sufficient recovery period following the onset. The hour the substorm occurs on will be referred to as the start of “Day 0” and the entire analysis period will be referred to as the “substorm interval.” All dates and times where the hourly AE index meets a threshold, and a substorm event occurs during the winter season in either polar region, were used in the following analysis. Winter season is defined as June, July, August for Southern Hemisphere (SH) and December, January, February for NH. When horizontal distributions of ozone were investigated for the SH case, only the SH winter season was used. Cases where multiple substorms occurred within the initially identified hour were counted as one epoch event. This is done in order to compile a list of times that will be used to investigate atmospheric changes (with ozone data then analyzed over 24 hr daily averaging windows), rather than compiling a complete list of substorms. Overall, when considering the winter season in both hemispheres, 1,558 events when one or more substorms occurred at the start of Day 0 were found.

Due to the high occurrence frequency of substorms, when investigating one substorm event, other substorms will likely occur within the 31-day substorm interval. Figure 1 shows the number of substorms occurring within each hour in the overall 31-day substorm interval. The start of Day 0 highlights our 1,558 epoch events, but we can see the increased number of substorms leading up to, and following this. It is clear the substorms are present throughout the 31 day period, but the highest occurrence is associated with Day 0.

Substorm EEP is expected to be limited to geomagnetic L-shells of around $L = 4$ – 9.5 , peaking between L of ~ 6 – 7 (Cresswell-Moorcock et al., 2013). To account for this, the geographic locations of the MLS and GOMOS ozone observations were mapped to geomagnetic (IGRF) L-shells, using standard field-line integration procedures (e.g.,

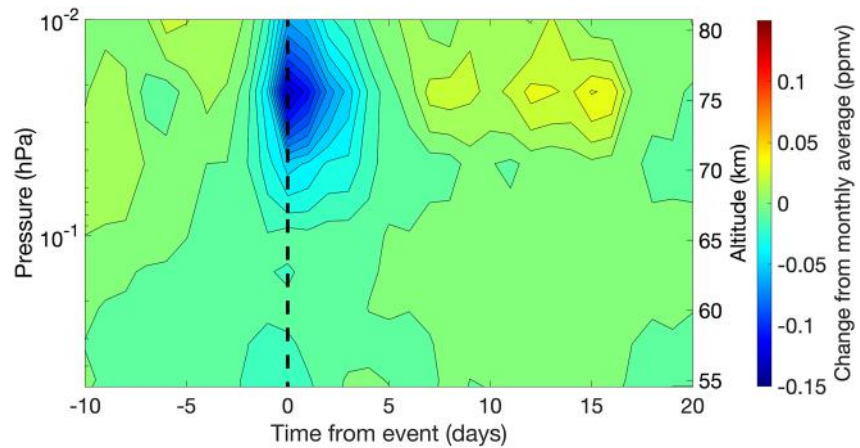


Figure 2. Mesospheric O₃ change from Microwave Limb Sounder observations based on 1,558 substorm epochs using AE ≥ 500 nT. The ozone data represents Northern Hemisphere and Southern Hemisphere winter seasons and has been averaged (mean) for L shells 4–7 and seasonally adjusted (see text for details). Contour intervals are 0.01 ppmv. The black dashed line indicates epoch day 0. Approximate vertical range in km is given on the right-hand y-axis.

Roederer, 1970). As there are much fewer satellite observations closer to the poles, the L-shell range of 4–7 has been chosen.

To ensure that the atmospheric impact is not dominated by potential geomagnetic storms taking place simultaneously to substorms, we checked the Dst and Kp indices for the substorm onset times. Median Dst index for the substorm events is −30 nT, with a lower quartile of −45 nT. Dst of −30 nT is known to correspond to typical substorm conditions (Gonzalez et al., 1994) and the lower quartile does not meet the Dst ≤ −50 nT threshold for storm conditions (Gonzalez et al., 1994; Rodger, Hendry, et al., 2022). Overall, approximately 80% of the substorm events analyzed have a corresponding Dst above the −50 nT threshold. The upper quartile for the Kp index is 4.7 (with median Kp of 4.0), which is below the threshold for minor geomagnetic storm conditions (Kp ≥ 5). To further ensure the analysis was not contaminated by a potential small number of geomagnetic storms, all data analysis was tested using mean and median averaging, with both methods providing consistent results in magnitude and overall response. This gives further confidence that our results are not contaminated by geomagnetic storms, but rather reflect the atmospheric response to substorm electron precipitation.

3. Results

First we examine MLS mean ozone observations averaged within L shells 4–7, for substorm events with an associated AE index ≥ 500 nT. L shells 4–7 are used here, as the satellite data coverage is better over lower geomagnetic latitudes, rather than extending to L = 9.5. The seasonally adjusted and L-shell averaged superposed epoch ozone results for polar winter months are shown in Figure 2. We find a prominent ozone decrease signal around Day 0, which is emphasized by the dashed black line. The peak reduction of ozone reaches 0.13 ppmv corresponding to an approximately 11% reduction (typical values are in the range of 1.1–1.3 ppmv), centered at 0.02 hPa level (~76 km altitude), in comparison to the analysis using random epochs which will be discussed shortly. The ozone loss between 60 and 80 km altitudes lasts roughly until epoch day 5, after which the values return to background levels. The ozone loss appears to start occurring before Day 0. This is consistent with Figure 1, which shows that substorm activity starts increasing 1–2 days before the peak at Day 0.

To test the statistical significance of the peak ozone loss seen in Figure 2, bootstrap resampling of the MLS data was applied with 10,000 repetitions. Figure 3 presents the results for the corresponding peak ozone loss pressure

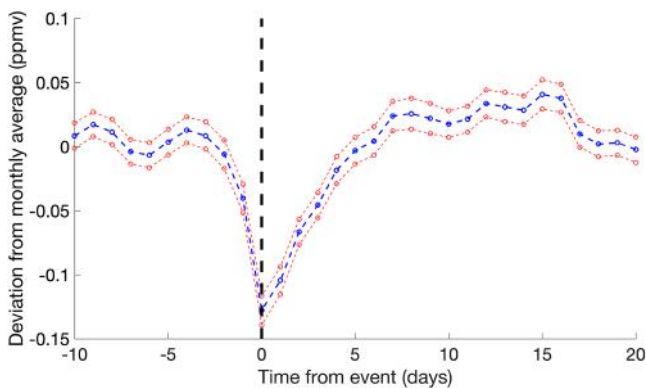


Figure 3. Slice through ozone data shown in Figure 2 at the 0.02 hPa pressure level (≈76 km), now focusing on the temporal evolution of the superposed epoch analysis (SEA) at the peak ozone loss pressure level. Bootstrap resampling of the Microwave Limb Sounder data was applied with 10,000 repetitions to estimate the 2 standard deviation error bars (red) for the SEA method.

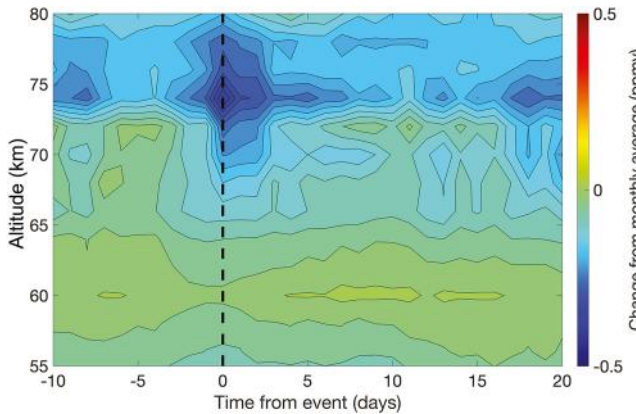


Figure 4. Mesospheric O₃ change from Global Ozone Monitoring by Occultation of Stars observations based on 1,080 substorm epochs using AE ≥ 500 nT. The ozone data represents winter season in each hemisphere and has been averaged (median) for L shells 4–7 and seasonally adjusted. Contour intervals are 0.03 ppmv. The black dashed line indicates epoch day 0. The vertical range in km is given on the y-axis.

level of 0.02 hPa (~76 km) with a 2 standard deviation (2σ) bootstrapping error estimate. Day 0 has an upper error band of -0.12 ppmv and a lower error band of -0.14 ppmv. The ozone reduction on Day 0 of the substorm interval is well beyond the 2σ error estimates on days before and after Day 0. This suggests that the observed ozone loss is statistically significant. To test the robustness of the ozone signal further, random 31 day intervals were generated to test our results using the SEA method. Five hundred and forty seven random epoch events were generated during the Arctic and Antarctic polar winter seasons. No dates were excluded in this process. The random epoch events were used were analyzed following the same method as was done for Figure 2. As can be seen from Figure S1, while a small amount of noise ($<\pm 0.05$ ppmv) is present in the randomly generated epochs, no strong signals comparable to Figure 2 is present here. This gives further confidence that the ozone loss signal in Figures 2 and 3 is linked to substorm-driven EEP.

In addition to the winter season, we further analyzed MLS ozone observations for other seasons (not shown). During the Arctic and Antarctic autumn seasons, we found an ozone loss signal that was qualitatively similar to that seen during winter, but much weaker, at about half of the magnitude seen in Figure 2. The signals during other seasons did not exceed the noise levels of our random test (± 0.05 ppmv). These results are in agreement with previous work on seasonal effects on EPP driven ozone loss (see e.g., Seppälä et al., 2015).

Figure 4 presents the SEA analysis of the GOMOS ozone observations. One thousand eighty epoch events were found in the time interval covered by GOMOS observations (note that both temporal and spatial coverage of the GOMOS data will differ from MLS). Here we see ozone loss around 75 km altitude taking place across the time period, with varying magnitudes. This is likely a result of higher overall substorm activity in the time period covered by GOMOS observations. Below 75 km altitude, mainly above 65 km ozone loss peaks following Epoch day 0, reaching over 0.2 ppm average ozone loss. By Day 5 ozone has recovered to background variability levels.

Both MLS (Figure 2) and GOMOS show that the ozone loss signal is focused above 65 km altitude. The overall onset and recover times of the peak ozone loss between 65 and 73 km are similar from the two satellite instruments, with GOMOS showing lower ozone values (higher loss) and more variability around 75 km. The main differences are likely a result of the difference in vertical resolution, and spatial and temporal coverage, of the two instruments. However, the overall agreement suggest that both observe ozone loss relating to substorm activity.

In addition to the L-shell averages, we further analyzed the horizontal distribution of the MLS ozone signal in the SH at 0.02 hPa (995 events). For each day in the substorm interval, the data was averaged (mean) into a 5° by 10° latitude–longitude grid. Each map in Figure 5 depicts a single day within the substorm interval during SH winter, with the epoch days indicated by the captions. The gray circles on the maps present L shells 4 (closest to the equator), 5, 6, and 7 (closest to the pole). There is little change from the monthly average 5 days before the zero epoch (Figure 5a). On Day 0 (Figure 5b) we see a clear pattern of ozone reduction, which remains present on Day 3 (Figure 5e). By Day 5 (Figure 5f) ozone has returned back to background levels. Note that in comparison to the L shell averages presented in Figure 2, here we observe larger regional ozone loss, peaking at nearly up to ~ 0.3 ppmv. This corresponds to about 21% reduction from the background. The ozone loss pattern largely follows the shape of L shells in the region poleward of 60° S. Equatorward of approximately 60° S this pattern is not observed and ozone levels remain similar to pre-Day 0 levels. The magnitude and duration of the ozone loss over the horizontal distribution is different to the L shell averages seen in Figure 2. The L shell average ozone loss on Day 3 is under 0.05 ppmv, while the horizontal distribution reveals regions of loss over 0.1 ppmv. This is consistent with what we can see in Figure 5: the ozone loss pattern is not present across all sectors of L shells 4–7, thus smaller overall reduction is observed when averaged over the whole L shell range.

The horizontal pattern in Figure 5 is consistent with Andersson, Verronen, Rodger, Clilverd, and Wang (2014), who analyzed horizontal distributions of OH observations from the same instrument (MLS) and found that EEP driven HO_x production peaked at high latitudes. Andersson, Verronen, Rodger, Clilverd, and Wang (2014) attributed the patterns partially to the presence of the South Atlantic Magnetic Anomaly, and partially to atmospheric

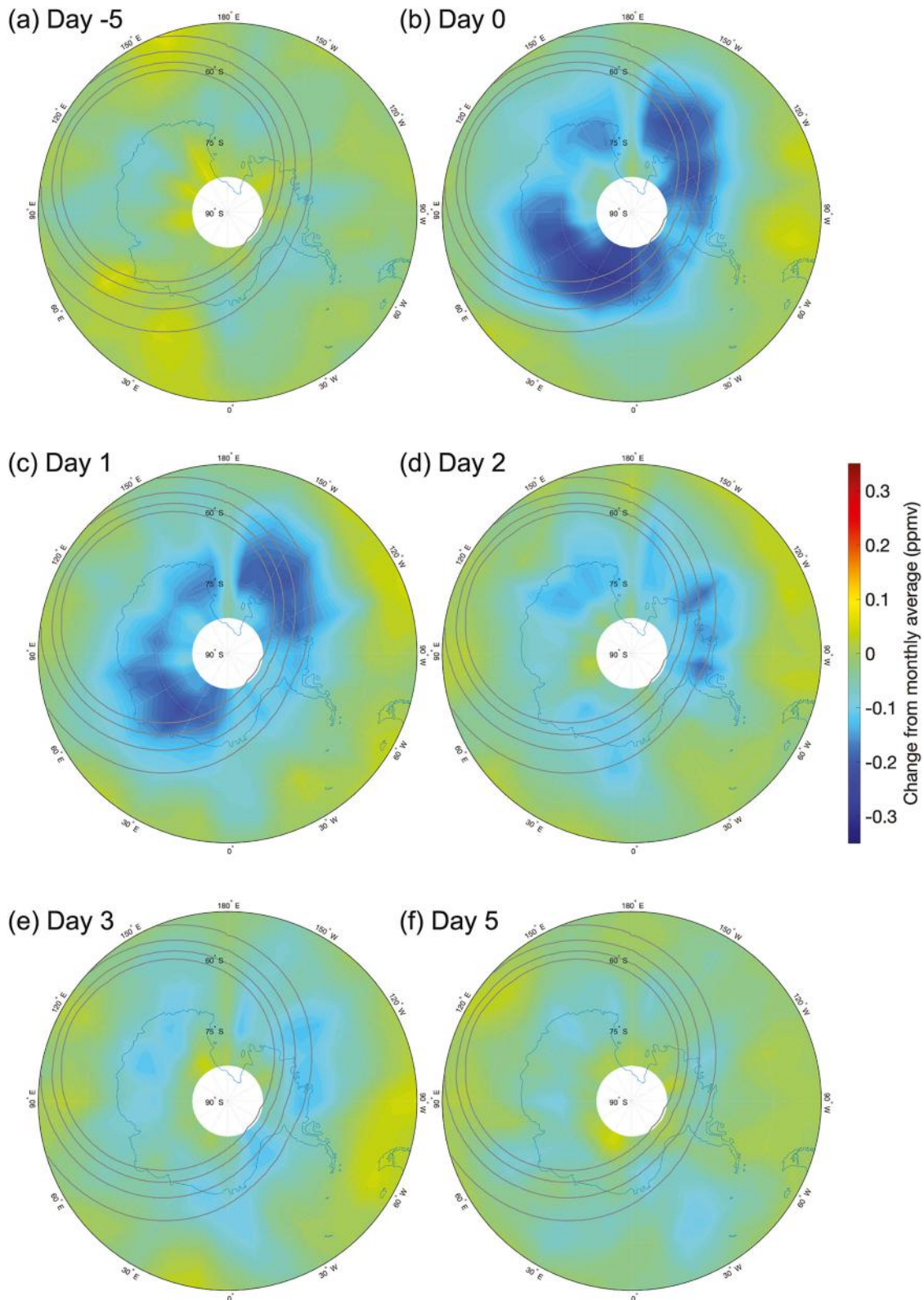


Figure 5. Southern Hemisphere polar winter O₃ change at 0.02 hPa level from Microwave Limb Sounder observations, based on 995 substorm epoch event using AE \geq 500 nT. Epoch days as shown in the captions. The ozone data was seasonally adjusted and adapted into a 5° by 10° latitude by longitude grid. Contour intervals are 0.01 ppmv. Maps were smoothed using 2D convolution filter function. The gray circles show L shells 4, 5, 6, and 7.

conditions, which favored HO_x production in the high polar latitudes, rather than in the L shell region that extends further toward the equator. As we expect the substorm driven ozone loss to be a result of initial HO_x production, the ozone loss patterns consistent with those of OH found by Andersson, Verronen, Rodger, Clilverd, and Wang (2014) support the cause of the ozone loss patterns in Figure 5 to be that of EEP, in our case driven by substorm activity. The results produced using ozone observations from the NH in winter, not included, resemble those seen in the SH.

4. Conclusion

Here, we provide the first ever observational evidence of mesospheric ozone depletion driven by EPP from magnetospheric substorms. The ozone loss is clearest during polar winter, a peak ozone loss of 9%–12% at 0.02 hPa pressure level (around 76 km altitude) is present in L shell averaged SEA. The loss lasts for around 5 days, before returning to background levels. When the horizontal ozone response is considered, we find up to 21% regional loss where the L shell band 4–7 corresponds to the highest (least illuminated) geographic latitudes in the SH. At the corresponding vertical level, Seppälä et al. (2015) simulated nighttime ozone loss of 20%–25%. Overall the observed response follows the shape of the L shell band, but ozone loss remains limited to latitudes poleward of 60°S. This is consistent with previous HO_x results presented by Andersson, Verronen, Rodger, Clilverd, and Wang (2014), which provides further evidence that the horizontal ozone loss pattern is a result of EEP driven by substorm activity.

These results now conclusively confirm the earlier modeling results of Seppälä et al. (2015): substorms are indeed an important source for ozone variability in the mesosphere. Representation of substorms in EEP proxies used in atmospheric and climate simulations (Matthes et al., 2017; van de Kamp et al., 2016) should be evaluated and a concerted effort to assure their inclusion is needed to provide realistic representation of atmospheric ozone variability.

Data Availability Statement

All the data used in this study is freely available from the following sources. SOPHIE: <https://supermag.jhuapl.edu/substorms/>, AE: <https://wdc.kugi.kyoto-u.ac.jp/dstae/>, Aura/MLS version 5 ozone observations: (Schwartz et al., 2020), GOMOS (requires free registration): https://earth.esa.int/eogateway/catalog/envisat-gomos-level-2-atmospheric-constituents-profiles-gom_nl__2p-, and SPE list: <https://umbra.nascom.nasa.gov/SEP/>.

References

- Akasofu, S. I. (1964). The development of the auroral substorm. *Planetary and Space Science*, 12(4), 273–282. [https://doi.org/10.1016/0032-0633\(64\)90151-5](https://doi.org/10.1016/0032-0633(64)90151-5)
- Andersson, M. E., Verronen, P. T., Rodger, C. J., Clilverd, M. A., & Seppälä, A. (2014). Missing driver in the Sun-Earth connection from energetic electron precipitation impacts mesospheric ozone. *Nature Communications*, 5(1), 5197. <https://doi.org/10.1038/ncomms6197>
- Andersson, M. E., Verronen, P. T., Rodger, C. J., Clilverd, M. A., & Wang, S. H. (2014). Longitudinal hotspots in the mesospheric OH variations due to energetic electron precipitation. *Atmospheric Chemistry and Physics*, 14(2), 1095–1105. <https://doi.org/10.5194/acp-14-1095-2014>
- Angelopoulos, V. (2008). The THEMIS mission. *Space Science Reviews*, 141(1), 5–34. <https://doi.org/10.1007/s11214-008-9336-1>
- Angelopoulos, V., Artemyev, A., Phan, T. D., & Miyashita, Y. (2020). Near-Earth magnetotail reconnection powers space storms. *Nature Physics*, 16(3), 317–321. <https://doi.org/10.1038/s41567-019-0749-4>
- Aryan, H., Sibeck, D., Balikhin, M., Agapitov, O., & Kletzing, C. (2016). Observation of chorus waves by the Van Allen Probes: Dependence on solar wind parameters and scale size. *Journal of Geophysical Research: Space Physics*, 121(8), 7608–7621. <https://doi.org/10.1002/2016ja022775>
- Cresswell-Moorcock, K., Rodger, C., Kero, A., Collier, A., Clilverd, M., Häggström, I., & Pitkänen, T. (2013). A reexamination of latitudinal limits of substorm-produced energetic electron precipitation. *Journal of Geophysical Research: Space Physics*, 118(10), 6694–6705. <https://doi.org/10.1002/jgra.50598>
- Davis, T. N., & Sugiura, M. (1966). Auroral electrojet activity index ae and its universal time variations. *Journal of Geophysical Research*, 71(3), 785–801. <https://doi.org/10.1029/JZ071i003p00785>
- Denton, M. H., Kivi, R., Ulich, T., Rodger, C. J., Clilverd, M. A., Horne, R. B., & Kavanagh, A. J. (2018). Solar proton events and stratospheric ozone depletion over northern Finland. *Journal of Atmospheric and Solar-Terrestrial Physics*, 177, 218–227. <https://doi.org/10.1016/j.jastp.2017.07.003>
- Fang, X., Randall, C. E., Lummerzheim, D., Solomon, S. C., Mills, M. J., Marsh, D. R., et al. (2008). Electron impact ionization: A new parameterization for 100 eV to 1 MeV electrons. *Journal of Geophysical Research*, 113(A9), A09311. <https://doi.org/10.1029/2008JA013384>
- Forsyth, C., Rae, I. J., Coxon, J. C., Freeman, M. P., Jackman, C. M., Gjerloev, J., & Fazakerley, A. N. (2015). A new technique for determining substorm onsets and phases from indices of the electrojet (SOPHIE). *Journal of Geophysical Research: Space Physics*, 120(12), 10592–10606. <https://doi.org/10.1002/2015ja021343>
- Friederich, F., Sinnhuber, M., Funke, B., von Clarmann, T., & Orphal, J. (2014). Local impact of solar variation on NO₂ in the lower mesosphere and upper stratosphere from 2007 to 2012. *Atmospheric Chemistry and Physics*, 14(8), 4055–4064. <https://doi.org/10.5194/acp-14-4055-2014>

Acknowledgments

KCS would like to thank The University of Otago for the Fanny Evans Postgraduate Scholarship For Women and the Otago publishing bursary, as well as the Zonta Metropolitan Club for the Women in STEM scholarship. We gratefully acknowledge the SuperMAG collaborators (<https://supermag.jhuapl.edu/info/?page=acknowledgement>). We acknowledge the substorm timing list identified by the SOPHIE technique (Forsyth et al., 2015), and the SuperMAG collaboration (Gjerloev, 2012). AS is grateful to Prof. Noora Partamies of UNIS for helpful discussion on substorms. Open access publishing facilitated by University of Otago, as part of the Wiley - University of Otago agreement via the Council of Australian University Librarians.

- Funke, B., Baumgaertner, A., Calisto, M., Egorova, T., Jackman, C. H., Kieser, J., et al. (2011). Composition changes after the Halloween solar proton event: The high energy particle precipitation in the atmosphere (HEPPA) model versus MIPAS data intercomparison study. *Atmospheric Chemistry and Physics*, *11*(17), 9089–9139. <https://doi.org/10.5194/acp-11-9089-2011>
- Funke, B., López-Puertas, M., Holt, L., Randall, C. E., Stiller, G., & von Clarmann, T. (2014). Hemispheric distributions and interannual variability of NO_y produced by energetic particle precipitation in 2002–2012. *Journal of Geophysical Research: Atmospheres*, *119*(23), 13565–13582. <https://doi.org/10.1002/2014JD022423>
- Gjerloev, J. W. (2012). The supermag data processing technique. *Journal of Geophysical Research*, *117*(A9), A09213. <https://doi.org/10.1029/2012JA017683>
- Gonzalez, W. D., Joselyn, J. A., Kamide, Y., Kroehl, H. W., Rostoker, G., Tsurutani, B. T., & Vasyliunas, V. M. (1994). What is a geomagnetic storm? *Journal of Geophysical Research*, *99*(A4), 5771–5792. <https://doi.org/10.1029/93JA02867>
- Jackman, C. H., Marsh, D. R., Vitt, F. M., Garcia, R. R., Randall, C. E., Fleming, E. L., & Frith, S. M. (2009). Long-term middle atmospheric influence of very large solar proton events. *Journal of Geophysical Research*, *114*(D11), D11304. <https://doi.org/10.1029/2008JD011415>
- Jackman, C. H., McPeters, R. D., Labow, G. J., Fleming, E. L., Praderas, C. J., & Russell, J. M. (2001). Northern hemisphere atmospheric effects due to the July 2000 solar proton event. *Geophysical Research Letters*, *28*(15), 2883–2886. <https://doi.org/10.1029/2001GL013221>
- Kauristie, K., Morschhauser, A., Olsen, N., Finlay, C. C., McPherron, R. L., Gjerloev, J. W., & Oppenorth, H. J. (2017). On the usage of geomagnetic indices for data selection in internal field modelling. *Space Science Reviews*, *206*(1–4), 61–90. <https://doi.org/10.1007/s11214-016-0301-0>
- Kyrölä, E., Tamminen, J., Leppelmeier, G. W., Sofieva, V., Hassinen, S., Bertaux, J. L., et al. (2004). GOMOS on Envisat: An overview. *Advances in Space Research*, *33*(7), 1020–1028. [https://doi.org/10.1016/S0273-1177\(03\)00590-8](https://doi.org/10.1016/S0273-1177(03)00590-8)
- Lockwood, M., Chambodut, A., Finch, I. D., Barnard, L. A., Owens, M. J., & Haines, C. (2019). Time-of-day/time-of-year response functions of planetary geomagnetic indices. *Journal of Space Weather and Space Climate*, *9*, A20. <https://doi.org/10.1051/swsc/2019017>
- Matthes, K., Funke, B., Andersson, M. E., Barnard, L., Beer, J., Charbonneau, P., et al. (2017). Solar forcing for CMIP6 (v3.2). *Geoscientific Model Development*, *10*(6), 2247–2302. <https://doi.org/10.5194/gmd-10-2247-2017>
- Nesse Tyssøy, H., Partamies, N., Babu, E. M., Smith-Johnsen, C., & Salice, J. A. (2021). The predictive capabilities of the auroral electrojet index for medium energy electron precipitation. *Frontiers in Astronomy and Space Sciences*, *8*, 714146. <https://doi.org/10.3389/fspas.2021.714146>
- Nesse Tyssøy, H., Sandanger, M. I., Ødegaard, L. K. G., Stadsnes, J., Aasnes, A., & Zawedde, A. E. (2016). Energetic electron precipitation into the middle atmosphere—Constructing the loss cone fluxes from MEPED POES. *Journal of Geophysical Research: Space Physics*, *121*(6), 5693–5707. <https://doi.org/10.1002/2016JA022752>
- Nesse Tyssøy, H., Sinnhuber, M., Asikainen, T., Bender, S., Clilverd, M. A., Funke, B., et al. (2022). HEPPA III intercomparison experiment on electron precipitation impacts: 1. Estimated ionization rates during a geomagnetic active period in April 2010. *Journal of Geophysical Research: Space Physics*, *127*(1), e2021JA029128. <https://doi.org/10.1029/2021JA029128>
- Newell, P. T., & Gjerloev, J. W. (2011a). Evaluation of supermag auroral electrojet indices as indicators of substorms and auroral power. *Journal of Geophysical Research*, *116*(A12), A12211. <https://doi.org/10.1029/2011JA016779>
- Newell, P. T., & Gjerloev, J. W. (2011b). Substorm and magnetosphere characteristic scales inferred from the supermag auroral electrojet indices. *Journal of Geophysical Research*, *116*(A12), A12232. <https://doi.org/10.1029/2011JA016936>
- Partamies, N., Juusola, L., Tanskanen, E., & Kauristie, K. (2013). Statistical properties of substorms during different storm and solar cycle phases. *Annales Geophysicae*, *31*(2), 349–358. <https://doi.org/10.5194/angeo-31-349-2013>
- Partamies, N., Tesema, F., Bland, E., Heino, E., Nesse Tyssøy, H., & Kallelid, E. (2021). Electron precipitation characteristics during isolated, compound, and multi-night substorm events. *Annales Geophysicae*, *39*(1), 69–83. <https://doi.org/10.5194/angeo-39-69-2021>
- Prather, M. J. (1981). Ozone in the upper stratosphere and mesosphere. *Journal of Geophysical Research*, *86*(C6), 5325. <https://doi.org/10.1029/JC086iC06p05325>
- Rodger, C. J., Clilverd, M. A., Hendry, A. T., & Forsyth, C. (2022). Examination of radiation belt dynamics during substorm clusters: Magnetic local time variation and intensity of precipitating fluxes. *Journal of Geophysical Research: Space Physics*, *127*(12), e2022JA030750. <https://doi.org/10.1029/2022JA030750>
- Rodger, C. J., Cresswell-Moorcock, K., & Clilverd, M. A. (2016). Nature's Grand Experiment: Linkage between magnetospheric convection and the radiation belts. *Journal of Geophysical Research: Space Physics*, *121*(1), 171–189. <https://doi.org/10.1002/2015JA021537>
- Rodger, C. J., Hendry, A. T., Clilverd, M. A., Forsyth, C., & Morley, S. K. (2022). Examination of radiation belt dynamics during substorm clusters: Activity drivers and dependencies of trapped flux enhancements. *Journal of Geophysical Research: Space Physics*, *127*(1), e2021JA030003. <https://doi.org/10.1029/2021JA030003>
- Roederer, J. G. (1970). *Dynamics of geomagnetically trapped radiation* (Vol. 2). Springer-Verlag. <https://doi.org/10.1007/978-3-642-49300-3>
- Sagi, K., Pérot, K., Murtagh, D., & Orsolini, Y. (2017). Two mechanisms of stratospheric ozone loss in the Northern Hemisphere, studied using data assimilation of Odin/SMR atmospheric observations. *Atmospheric Chemistry and Physics*, *17*(3), 1791–1803. <https://doi.org/10.5194/acp-17-1791-2017>
- Schwartz, M., Froidevaux, L., Livesey, N., & Read, W. (2020). *MLS/Aura level 2 ozone (O₃) mixing ratio V005*. Goddard Earth Sciences Data and Information Services Center (GES DISC). <https://doi.org/10.5067/Aura/MLS/DATA2516>
- Seppälä, A., Clilverd, M. A., Beharrell, M. J., Rodger, C. J., Verronen, P. T., Andersson, M. E., & Newnham, D. A. (2015). Substorm-induced energetic electron precipitation: Impact on atmospheric chemistry. *Geophysical Research Letters*, *42*(19), 8172–8176. <https://doi.org/10.1002/2015GL065523>
- Seppälä, A., Matthes, K., Randall, C. E., & Mironova, I. A. (2014). What is the solar influence on climate? Overview of activities during CAWSES-II. *Progress in Earth and Planetary Science*, *1*, 24. <https://doi.org/10.1186/s40645-014-0024-3>
- Seppälä, A., Verronen, P. T., Sofieva, V. F., Tamminen, J., Kyrölä, E., Rodger, C. J., & Clilverd, M. A. (2006). Destruction of the tertiary ozone maximum during a solar proton event. *Geophysical Research Letters*, *33*(7), L07804. <https://doi.org/10.1029/2005GL025571>
- Sinnhuber, M., Friederich, F., Bender, S., & Burrows, J. P. (2016). The response of mesospheric NO to geomagnetic forcing in 2002–2012 as seen by SCIAMACHY. *Journal of Geophysical Research: Space Physics*, *121*(4), 3603–3620. <https://doi.org/10.1002/2015JA022284>
- Sofieva, V. F., Kyrölä, E., Verronen, P. T., Seppälä, A., Tamminen, J., Marsh, D. R., et al. (2009). Spatio-temporal observations of the tertiary ozone maximum. *Atmospheric Chemistry and Physics*, *9*(13), 4439–4445. <https://doi.org/10.5194/acp-9-4439-2009>
- Tamminen, J., Kyrölä, E., Sofieva, V. F., Laine, M., Bertaux, J. L., Hauchecorne, A., et al. (2010). Gomos data characterisation and error estimation. *Atmospheric Chemistry and Physics*, *10*(19), 9505–9519. <https://doi.org/10.5194/acp-10-9505-2010>
- Turunen, E., Verronen, P. T., Seppälä, A., Rodger, C. J., Clilverd, M. A., Tamminen, J., et al. (2009). Impact of different energies of precipitating particles on NO_x generation in the middle and upper atmosphere during geomagnetic storms. *Journal of Atmospheric and Solar-Terrestrial Physics*, *71*(10–11), 1176–1189. <https://doi.org/10.1016/j.jastp.2008.07.005>

- van de Kamp, M., Seppälä, A., Clilverd, M. A., Rodger, C. J., Verronen, P. T., & Whittaker, I. C. (2016). A model providing long-term datasets of energetic electron precipitation during geomagnetic storms. *Journal of Geophysical Research: Atmospheres*, *121*(20), 12520–12540. <https://doi.org/10.1002/2015JD024212>
- Wing, S., Gkioulidou, M., Johnson, J. R., Newell, P. T., & Wang, C.-P. (2013). Auroral particle precipitation characterized by the substorm cycle. *Journal of Geophysical Research: Space Physics*, *118*(3), 1022–1039. <https://doi.org/10.1002/jgra.50160>
- Zhang, X. J., Thorne, R., Artemyev, A., Mourenas, D., Angelopoulos, V., Bortnik, J., et al. (2018). Properties of intense field-aligned lower-band chorus waves: Implications for nonlinear wave-particle interactions. *Journal of Geophysical Research: Space Physics*, *123*(7), 5379–5393. <https://doi.org/10.1029/2018ja025390>